Accelerator and beam conditions critical for physics and detector simulations for the Electron-Ion Collider

Jaroslav Adam[1], Elke-Caroline Aschenauer[1], Markus Diefenthaler[2], Yulia Furletova[2], Jin Huang[1], Alexander Jentsch[1], and Brian Page[1]

[1]Brookhaven National Laboratory, Upton, New York 11973, USA
[2]Thomas Jefferson National Accelerator Facility, Newport News, Virginia 23606, USA

July 11, 2021

Abstract

We identify accelerator and beam conditions at the Electron-Ion Collider (EIC) that need to be included in physics and detector simulations. For our studies, we implement accelerator and beam effects in the Pythia 8 Monte Carlo event generator and examine their influence on the measurements in the central and far-forward regions of the detector. In our analysis, we demonstrate that the accelerator and beam effects can be also studied accurately by modifying the Monte Carlo input to detector simulations, without having to implement the effects directly in the event generators.

1 Interaction Regions at the Electron-Ion Collider

The present interaction region (IR) and detector designs for the Electron-Ion Collider (EIC) are the result of considerations which fulfill all of the below requirements:

- Versatile center-of-mass energy, E_{CM}, within the range of $30\,\text{GeV}$ to $140\,\text{GeV}$.

- A luminosity of up to $10^{34}\,\text{cm}^{-2}\,\text{s}^{-1}$.

- High polarization of electron and light ion beams with arbitrary spin patterns, with time-averaged polarization of up to 70%.

- Beam divergences at the interaction point (IP) and apertures of the interaction region magnets that are compatible with the acceptance requirements of the colliding beam detector.

- Collisions of electrons with a large range of light to heavy ions (protons to uranium ions).

- Up to two interaction regions.

To realize these requirements a couple of design choices have been made, which need to be included in the physics and detector simulations to get the most accurate description. The purpose of the interaction region is to focus the beams to small spot sizes at the collision point and to separate them into their respective beam lines while providing the space and geometry required by the physics program for the detector. The separation is accomplished by a total crossing angle of 25 mrad (or 35 mrad) between the two beams, which has the advantage of avoiding the introduction of separator

dipoles in the detector vicinity that would generate a substantial amount of synchrotron radiation. The detrimental effects of this crossing angle on the luminosity and beam dynamics are compensated by a crab-crossing scheme.

The layout of the EIC interaction region (IR) fulfills the following requirements:

- To achieve high luminosity, small transverse beam sizes are required. The beams are strongly focused at the interaction point (IP, small β^*) by low-β-quadrupole magnets (also referred to as final focusing quadrupoles).

- The final focusing quadrupoles must have sufficient aperture for the large beam size at their location.

- The colliding beam detector requires a large acceptance of protons scattered off the collision point. Therefore, we do not place accelerator components inside the detector. Some of the low-β quadrupoles have even larger apertures so scattered protons and neutrons can be detected by detector elements placed further downstream.

- The beam divergence (and the minimum β^*) is restricted to enable detection of forward scattered protons with transverse momentum as small as $200\,\mathrm{MeV}$. These particles are then outside the $10\,\sigma$ proton beam envelope and are detectable by near-beam-detectors, "Roman Pots", which are placed along the forward hadron beam pipe.

- The beams collide under a crossing angle of $25\,\mathrm{mrad}$ at IP-6 and $35\,\mathrm{mrad}$ at IP-8 to provide immediate separation of the electron and proton beams, to avoid parasitic collisions and to provide space for a neutron detector at zero degrees in the forward (hadron-going) direction and the luminosity detector on the rear (electron-going) side where the electrons exit. An important factor is the large bunch frequency (up to $99\,\mathrm{MHz}$, which corresponds to only $10\,\mathrm{ns}$ bunch spacing) required for high luminosity. The crossing angle effects (enlarged transverse beam size and excitation of synchro-betatron resonances) must be compensated for by using crab cavities, transverse RF resonators which kick the head and the tail of the proton (and electron) bunches in opposite directions in the plane of the crossing angle. These cavities are placed at a horizontal betatron phase advance of $\pi/2$ from the IP on both the rear and the forward sides, forming a $180°$ bump. This causes the bunches to be tilted in the horizontal plane by exactly half the crossing angle at the IP, and provides (ideally) the same collision geometry as head-on collisions and thereby avoids synchrobetatron coupling.

- Strong synchrotron radiation, which might be generated by the electron beam, can destroy sensitive detector equipment and make data-taking impossible. Therefore, we argue that the electron beam must not experience dipole fields in the IR, and certainly not upstream of the IP on the forward side. This is another strong reason why the two beams must collide at a crossing angle. Synchrotron radiation generated in the low-β quadrupoles on the rear-electron side should be absorbed on the rear side of the IR as far as possible from the detector so as to minimize backscattered photons. This requires an extra large aperture for the electron low-β quadrupole magnets on the downstream side of the IP. In addition it requires the detector solenoid axis to be aligned with the lepton beam.

- The IR layout must provide room for a luminosity monitor on the rear side. This monitor detects hard γ-rays that are generated in the Bethe-Heitler process, which are exploited for the luminosity measurement. The dipole magnet bending the electrons away from the path of the γ beam is at the same time a spectrometer magnet for the off-momentum electrons generated at low Q^2.

- On the forward proton side, a neutron spectrometer is required. A dipole magnet bends the hadron beam away from the collision axis to provide space for this element. It also generates
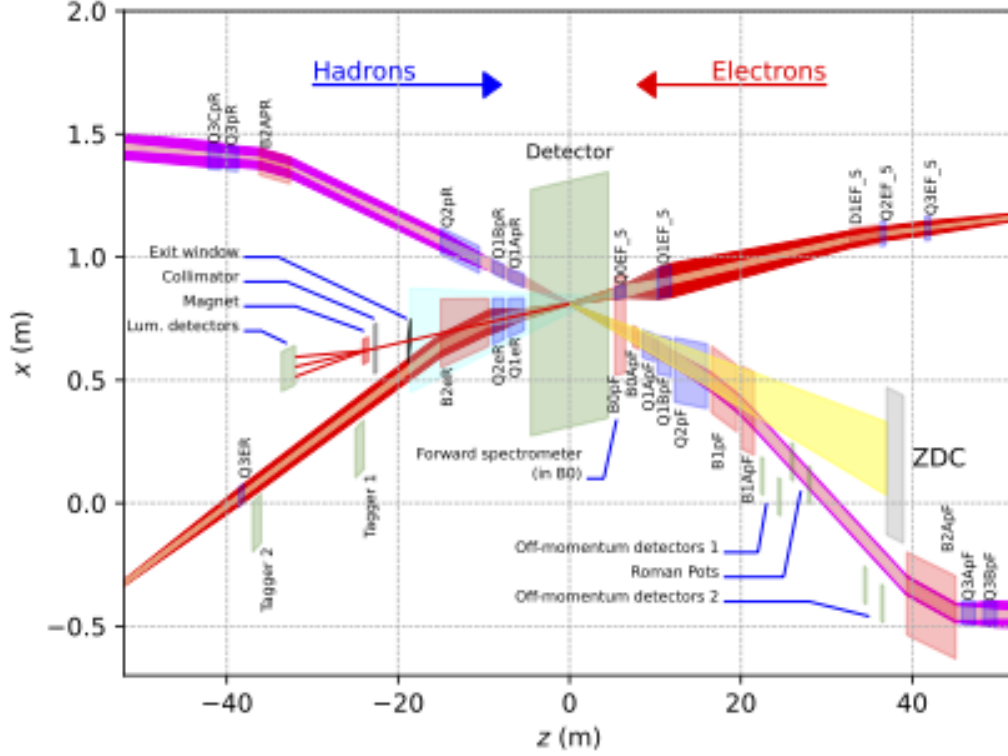
Figure 1: Schematic layout of the interaction region (top view, as simulated for high divergence, no cooling). Beams cross with a crossing angle of 25 mrad. Note the length scales for the horizontal and vertical axis are very different. The IR design integrates focusing magnets for both beams, luminosity and neutron detectors, electron taggers, spectrometer magnets, near-beam detectors (Roman pots for hadrons), crab cavities, and spin rotators for both beams. **Note: Beams cross with a crossing angle of 25 mrad, on the collision and tunnel floor the lepton beam has 8 mrad and the hadron beam 17 mrad angle. But in the experiment the solenoid axis is aligned with the electron beam, such the hadron beam is under 25 mrad.**

dispersion which helps to detect forward scattered protons in detectors that are integrated into the hadron beam pipe (called "Roman Pots"). At the 2nd IR, in addition, a secondary focus has been implemented in the outgoing hadron beam after the Roman Pots.

Figure 1 shows a schematic layout of the IR at IP-6 realizing all the requirements described above. The IR layout follows a right handed coordinate system, positive x ring inside, positive y upwards, positive z along the hadron beam. Figure 2 shows a schematic layout of the 2nd IR at IP-8 following all requirements described above and integrating a 2nd focus. Also this IR layout follows a right handed coordinate system, positive x ring inside, positive y upwards, positive z along the z-axis.

Note: Many of the detailed numbers discussed in the following sections are summarized in Tables 3.3 to 3.5 of the Conceptual Design Report for the EIC.
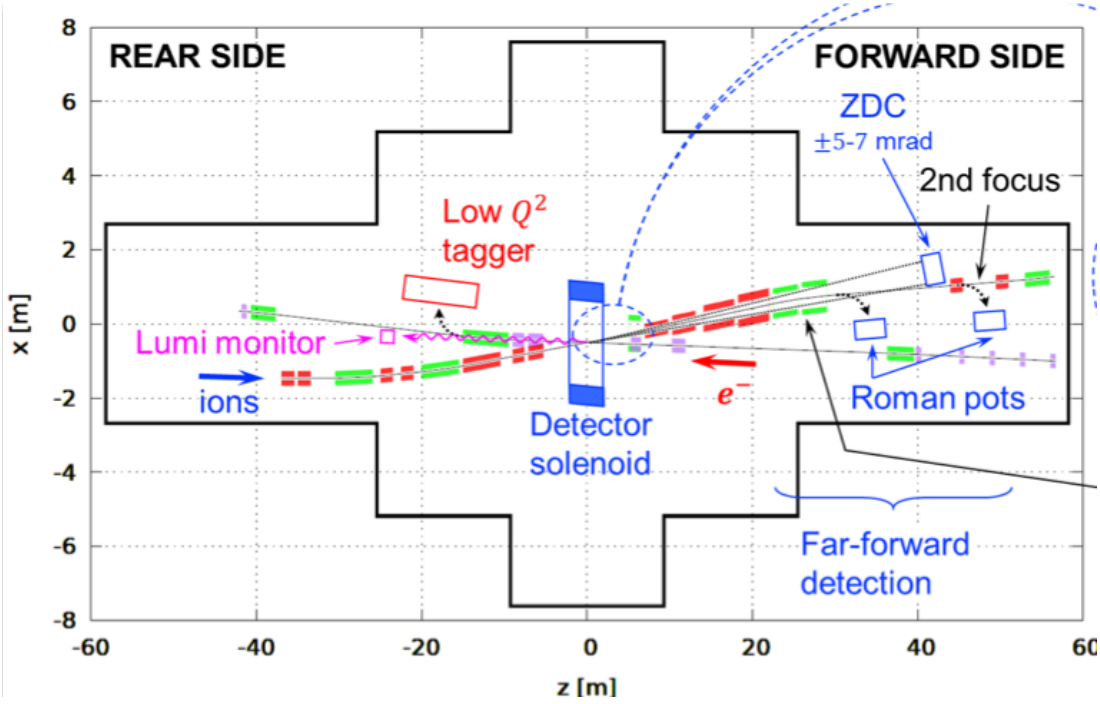
Figure 2: Schematic layout of the 2nd interaction region in IP-8. Beams cross with a crossing angle of 35 mrad. Note the length scales for the horizontal and vertical axis are very different. The IR design integrates focusing magnets for both beams, luminosity and neutron detectors, electron taggers, spectrometer magnets, near-beam detectors (Roman pots for hadrons), crab cavities, and spin rotators for both beams. **Note: Beams cross with a crossing angle of 35 mrad, on the collision and tunnel floor the lepton beam has 8 mrad and the hadron beam 27 mrad angle. Also for this IR the experiment the solenoid axis is aligned with the electron beam, such the hadron beam is under 35 mrad.**

2 Effects to the considered in physics and detector simulations

In this section, we describe accelerator and beam effects and their impact on the measurements in the central and far-forward detectors:

- **Impact of the Crossing Angle θ_{CA} (Central and Far-Forward Detectors)**
  The crossing angle introduces an p_T component to the incoming beams in the the x-direction of $\Delta P_T^x = P_z^{Beam} * sin(\theta_{CA})$. With the solenoid being aligned with the lepton beam the effect is all in the hadron beam for the central detector. The crossing angle also leads to a reduction of the z-component of the beam $\Delta P_z = P_z^{Beam} * cos(\theta_{CA}) - P_z^{Beam}$. In addition as the beams are not any longer back-to-back the bending power on the outgoing hadron beam side is not symmetric and one gets a strong functional azimuthal asymmetry of the acceptance at high rapidity $\eta \sim 4$.

- **Impact of the Crab Cavities (Central and Far-Forward Detectors)**
  The hadron bunch "rotation" at the IP is due to the crab cavities. Crabbing implies a transverse momentum kick $p_x(z)$ to the particle bunch, with the kicking strength proportional to the longitudinal position z of particles in the bunch. Therefore at the IP particles at the "head" of the bunch will have a slightly different orientation and/or transverse offset compared to the ones in the "tail" of the bunch, which leads to additional smearing of the apparent scattering

4

Parameter	unit	value	note
θ_c	rad	0.025	full crossing angle
E_b	eV	$275/100/41 \times 10^9$	beam energy
ω	Hz	1.23×10^9	angular frequency $\omega = 2\pi f$, f is the frequency of the crab cavity
β_{crab}	m	$1300/500/200$	beta function at crab cavity, three numbers corresponds to three energies respectively
β^*	m	0.9	beta function at IP
ϕ_{crab}	degree	90	crab cavity phase advance for ideal case. Actual lattice has mall deviations within 2.5 degree
k	1/m	4.13	wave number $= 1/$(wavelength of cavity)

Table 1: Parameter list for 197 MHz crab cavity for HSR

angle. The transverse momentum kick can be expressed as

$$p_x\left(z\right) = \frac{eE_0}{\omega} \sin\left(kz\right) \sin\left(\frac{kL}{2}\right) \sin\phi_{crab} \approx \frac{eE_0 z}{c} \sin\left(\frac{kL}{2}\right) \sin\phi_{\text{crab}} \tag{1}$$

where E_0 is the amplitude of the electric field acting on the bunch, ω and k are the angular frequency and the wave number of the crab cavity respectively, L is the bunch length, and ϕ_{crab} is the phase advance of the crab cavity. The longitudinal coordinate z is referencing to the center of the bunch, where $z = 0$.

For beam energy of E_b, transverse oscillation translates the longitudinally dependent kick p_x to a transverse offset x_{IP} at the interaction point (IP), which gives

$$x_{IP} = R_{12}\frac{p_x c}{E_b} = \sqrt{\beta_{crab}\beta^*}\frac{eE_0 z \sin\left(\frac{kL}{2}\right)\sin\phi_{crab}}{E_b} \tag{2}$$

where R_{12} is the element of transverse transfer matrix from the crab cavity to the IP, β_{crab} and β^* are the beta functions at the crab cavity and IP. These equations can be simplified, the required crabbing voltage is given by

$$V = \frac{cE_b\theta_c}{2e\omega\sqrt{\beta_{crab}\beta^*}\sin\phi_{crab}}, \tag{3}$$

and the transverse offset x_{IP} at the interaction point (IP) w.r.t the longitudinal position z in the bunch (center of bunch $z = 0$) by

$$x_{IP}(z) = \frac{\theta_c}{2k}\sin\left(kz\right), \tag{4}$$

and the transverse kick at the crab cavity location

$$\Delta x'_{CC} = x_{IP}/\sqrt{\beta_{crab}\beta^*}. \tag{5}$$

5

Parameter	unit	value	note
θ_c	rad	0.025	full crossing angle
E_b	eV	$18/10/5 \times 10^9$	beam energy
ω	Hz	2.46×10^9	angular frequency $\omega = 2\pi f$, f is the frequency of the crab cavity
β_{crab}	m	150 (may increase later)	beta function at crab cavity, currently it is the same for all energies
β^*	m	0.9	beta function at IP
ϕ_{crab}	degree	90	crab cavity phase advance for ideal case. Actual lattice has mall deviations within 2.5 degree
k	1/m	8.26	wave number $= 1/$(wavelength of cavity)

Table 2: Parameter list for 394 MHz crab cavity for ESR

The parameters needed to do these calculations listed trough out the EIC CDR are summarized for the hadron and electron crab cavities in Tab. 1 and 2.

The z-vertex determination of the event provided by the main tracker as well as high-resolution timing of the Roman Pot silicon sensors (of an order of $\sim 30\,\mathrm{ps}$) is able to fully mitigate this effect.

- **Impact of the Beam Energy Spread (Central and Far-Forward Detectors)**
  The beam energy of both beams is not a fixed number, but has a spread, which is gaussian with a width (RMS) of $\sim 10^{-4}$. The variation of the Beam energy along z is modified like $\Delta P_z^{smear} = P_z^{Beam} * \sigma_{RMS}$, this impacts also the beam energy modifications due to the crossing angle $\Delta P_T^x = (P_z^{Beam} + P_z^{smear}) * sin(\theta_{CA})$ and $\Delta P_z = (P_z^{Beam} + P_z^{smear}) * cos(\theta_{CA}) - P_z^{Beam}$.

- **Impact of the Angular Beam Divergence θ_{BD} (Central and Far-Forward Detectors)**
  The angular divergence $\sigma_{\theta_{BD}} = \sqrt{\epsilon_n/(\beta^* \gamma)}$ of the beam, with ϵ_n the normalized beam emittance and $\beta^*_{x,y}$ the β-function at the IP, is the Angular "spread" of the beam away from the central trajectory. It leads to a small initial transverse momentum to the beam particles, which can be expressed both in x and y by $(P_z^{Beam} + P_z^{smear}) * sin(\theta_{BD}^{x,y})$.

- **Impact of the Bunch Length (Central and Far-Forward Detectors)**
  Both beam bunches have an extended longitudinal length. These bunch lengths lead to an extended vertex distribution in z. The finite width of the vertex distribution at the IP adds uncertainty in the angle determination. This uncertainty can be eliminated by determining the vertex of the event through other tracks in the event being registered in the main detector and benefit from the excellent vertex definition from the μ-vertex detector. Detectors with sufficient timing resolution also help to isolate the location of the collision within the bunch, which is also important for the calculation of the crab cavity momentum kick, as expressed above.

We list useful relations for the discussions in the following sections:

- Transverse beam size at a certain location in z: $\sigma_{x,y}^z = \sqrt{\epsilon_n(\beta_{x,y}^z \gamma)}$.

- High divergence beams: smaller β^* at IP $\rightarrow$ higher Luminosity, but bigger β along $z \rightarrow$ worse low p_T acceptance at Roman Pots.

- Small divergence beams: larger β^* at IP $\rightarrow$ lower Luminosity, but smaller β along $z \rightarrow$ higher low p_T acceptance at Roman Pots.

3 Implementation

We have developed two methods for simulating the beam effects detailed in Sec. 2, one that utilizes the internal functionality of PYTHIA-8 and another that is applied as an after-burner to the output of any Monte Carlo event generator (MCEG). Both methods account for the perturbations to beam momenta due to crossing angle, divergence, and crab cavity impact and then boost and rotate the beam and final state particles into a frame in which the lepton beam lies along the z-axis. The details of the PYTHIA-8 and after-burner implementations are presented in sections 3.1 and 3.2, respectively, while a comparison of the methods along with a discussion of their complementarity can be found in Sec. 3.3. Section 3.4 describes an independent evaluation of the interaction vertex position based on a transport model and includes a comparison of the vertex distribution widths from the transport model and PYTHIA-8 implementation. In Appendix A, we give references to the source code of both methods.

3.1 PYTHIA-8 Implementation

The PYTHIA-8 implementation of EIC beam effects makes use of the internal BeamShape class, which provides significant flexibility in the choice of beam momentum components and interaction vertex coordinates. To utilize this functionality, the user declares a class deriving from the BeamShape base class and overloads the virtual pick() method. Within the pick() method, the user sets ten variables that specify the deviation of the xyz components of the momenta of the two beams from their nominal values as well as the position and time of the collision vertex. The BeamShape class also incorporates a random number generator so that beam effects characterized by a certain range can be sampled appropriately without having to re-initialize the simulation.

The beam effects model used in this analysis treats both the space-time position of the collision vertex and the changes in beam momentum due to beam energy spread, crossing angle, divergence, and crabbing effects. The procedure for simulating the position and time of the collision vertex is outlined in Fig. 3. It is assumed that both the hadron and lepton bunches are rotated by half of the beam crossing angle from their direction of travel in the xz plane and that they stay in a fixed orientation throughout their crossing.

1. Randomly choose the z positions of the interacting hadron and electron within their respective bunches. Assume the distribution of particles is gaussian in z with a sigma given by the RMS bunch length in the CDR

2. Propagate bunches in time until the interacting particles overlap. This sets the z and time coordinates of the collision as well as an 'offset' in x.

3. Randomly sample a position in x and y. The x and y overlap widths are assumed to be gaussian with a sigma given by $\sigma_e \sigma_p / \sqrt{\sigma_e^2 + \sigma_p^2}$ where $\sigma_{e,p} = \sqrt{\beta_{e,p}^* \epsilon_{e,p}}$ and the beta and emittance values are taken from the CDR. Add this x position to the offset found in the previous step. The x, y, z, and time are then set in the 'accelerator frame'.

4. Rotate the vertex coordinates into the 'detector frame' in which the z-axis is aligned with the lepton beam.

(a) Bunches Before Collision

(b) Bunches Interacting

(c) Collision Configuration

(d) Rotating Coordinates

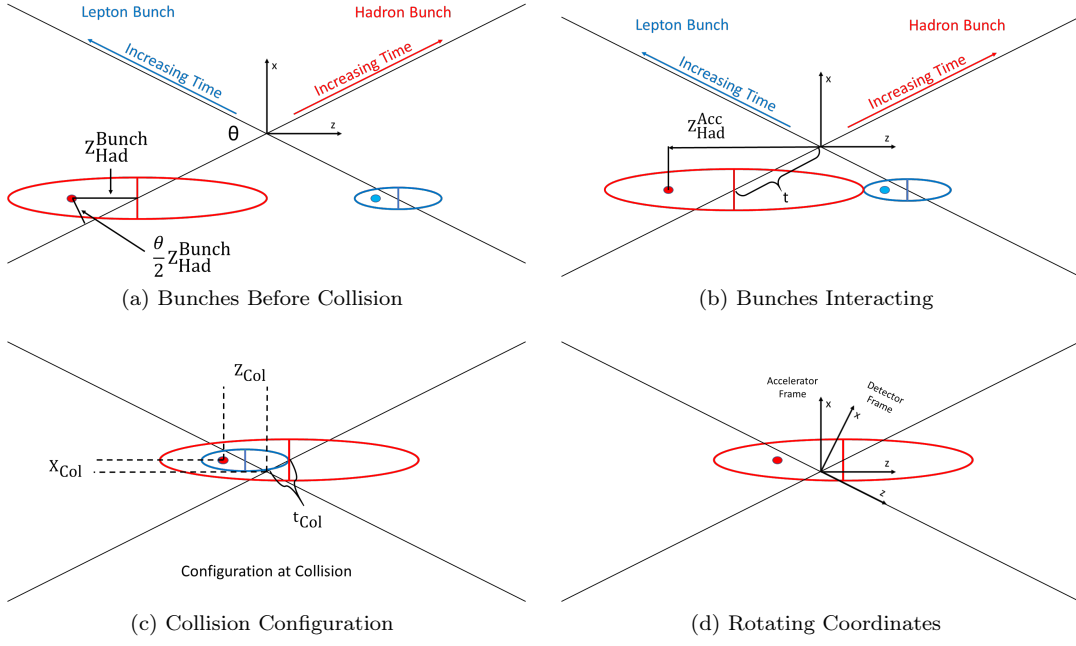Figure 3: Illustration of the collision model used to determine the interaction vertex time and position.

The z-position of the interacting hadron or lepton as a function of time in the accelerator frame is given by the equations (see Fig.):

$$z_{\text{Had}}^{\text{Acc}} = \text{Cos}\left(\frac{\theta}{2}\right) \times t + z_{\text{Had}}^{\text{Bunch}} \tag{6}$$

$$z_{\text{Lep}}^{\text{Acc}} = -\text{Cos}\left(\frac{\theta}{2}\right) \times t + z_{\text{Lep}}^{\text{Bunch}}, \tag{7}$$

where $z_{\text{Had}}^{\text{Acc}}$ and $z_{\text{Lep}}^{\text{Acc}}$ are the z positions of the colliding hadron and lepton in the accelerator frame, respectively, θ is the crossing angle, t is the time with respect to the moment the nominal centers of the bunches overlap (measured in millimeters with $c = 1$), and $z_{\text{Had}}^{\text{Bunch}}$ and $z_{\text{Lep}}^{\text{Bunch}}$ are the positions of the colliding hadron and lepton in relation to the center of their respective bunches. The collision occurs when $z_{\text{Had}}^{\text{Acc}} = z_{\text{Lep}}^{\text{Acc}}$, and then Eqs. 6 and 7 can be solved to find the z-position, time, and x-position (of the center-line of the bunches) of the collision occurred:

$$t_{\text{Col}} = \frac{\left(z_{\text{Lep}}^{\text{Bunch}} - z_{\text{Had}}^{\text{Bunch}}\right)}{2 \times \text{Cos}\left(\frac{\theta}{2}\right)} \tag{8}$$

$$z_{\text{Col}} = \frac{\left(z_{\text{Lep}}^{\text{Bunch}} + z_{\text{Had}}^{\text{Bunch}}\right)}{2} \tag{9}$$

$$x_{\text{Col}} = t_{\text{Col}} \times \text{Sin}\left(\frac{\theta}{2}\right). \tag{10}$$

The x, y, z, and t positions of the collision vertex can be seen in Fig. 4 for beam energies of 18x275 GeV and 5x41 GeV and crossing angles of 25 and 35 milliradians. The y, z, and t, vertex
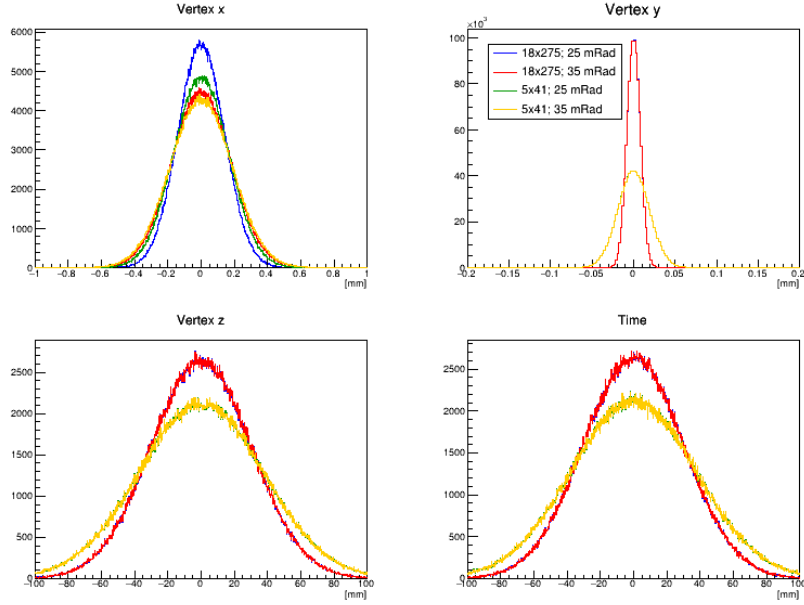
Figure 4: Detector frame vertex position and time distributions for beam energies of 18x275 GeV and 5x41 GeV and crossing angels of 25 and 35 milliradians.

distributions are somewhat wider at lower energy and insensitive to crossing angle. However, the degeneracy in crossing angle is broken for the x-vertex position, with the larger crossing angle corresponding to wider distributions. Correlations between vertex coordinates are also captured. Figure 5 shows little relationship between the x and z vertex positions in the Detector Frame, but if the z-position and time of the vertex can be measured independently and summed, a much tighter correlation with the x-position is found.

(a) Vertex X Vs Z

(b) Vertex X Vs Z+T

Figure 5: Correlations between the x and z positions (a) and the x and $Z + T$ sum (b) of the interaction vertex. In each panel, the upper row is 18x275 GeV and bottom row is 5x41 GeV beam energies and the left and right columns are 25 and 35 milliradian crossing angle, respectively.

With the vertex coordinates determined, the next step is to evaluate the effects on the incoming beam momenta, which then impact the final state particle distributions. As listed in Sec. 2, there

9

are four effects which impact the momenta of the incoming beams: the beam energy spread, crossing angle, beam divergence, and crab cavity kick. The change in the longitudinal momentum (energy) of the beam is determined first, as the beam energy affects the magnitude of the other contributions. The change in beam energy is determined by randomly sampling a gaussian distribution with a width given by the RMS $\Delta p/p$ values in Tabs. 3.3 and 3.4 in the CDR. The effect of the beam energy variation on the center-of-mass collision energy can be seen in Fig. 6 for four beam energy and crossing angle combinations. The slight offsets seen in the mean of the energy difference distributions is due to the crossing angle while the widths are dominated by the beam energy variation. The divergence and crab cavity kick also contribute to the width, but the effect is highly sub-dominant.
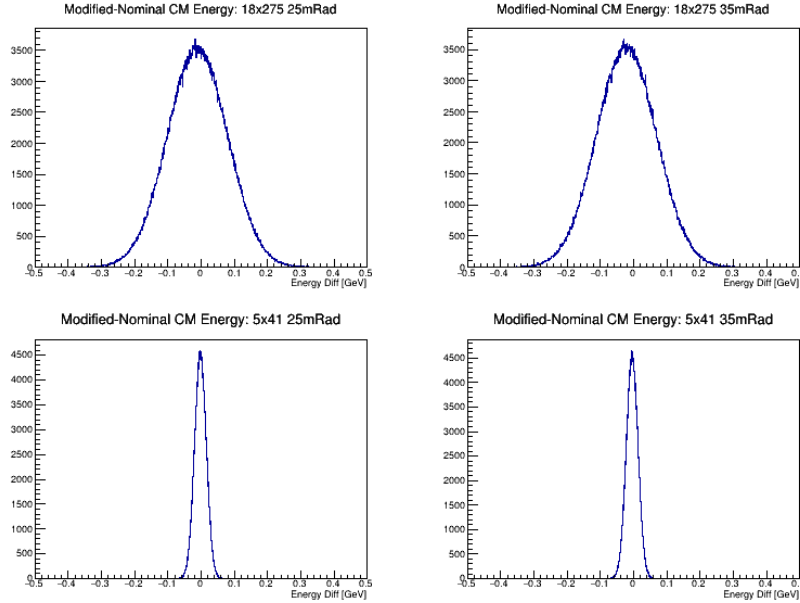

Figure 6: Difference in nominal vs modified center-of-mass energy due to the simulated beam effects for the 18x275 GeV 25 mRad (upper left), 18x275 GeV 35 mRad (upper right), 5x41 GeV 25 mRad (lower left), and 5x41 35 mRad (lower right) configurations.

The dominant perturbation on the incoming beam momenta and final state particle distributions comes from the crossing angle between the beams in the xz plane. In the current machine design, the beams cross at angles of 25 and 35 milliradians at IP6 and IP8, respectively. As the solenoid of the central detector will be aligned with the lepton beam, this is taken as the z-axis of our coordinate system and the hadron beam therefore takes the full crabbing angle. Thus, there is no change in the momentum of the lepton beam due to the crossing angle, while the hadron beam recieves a kick in the x direction with a magnitude given by the beam energy multiplied by the Sine of the full crossing angle. The reduction of the z component of the hadron beam momentum by Cosine of the crossing angle is also taken into account. It should be noted that the latest machine designs envision a vertical tilt of the electron storage ring. At IP6, this works out to a 100 microradian tilt in the y direction with the electron beam going to higher y in the outgoing lepton direction. This crossing angle is also 'transferred' to the hadron beam and contributes a momentum kick in the y direction, but due to the small size of the effect, is neglected in the treatment of the longitudinal beam momentum.

The angular beam divergence represents a deviation from parallel beam particle trajectories and introduces x and y momentum components into both the incoming lepton and hadron beam momenta. The sizes of the momentum perturbations in the frame of the beam are simply given by

the beam energy multiplied by Sine of the horizontal or vertical beam divergence angle. This angle has a characteristic width indicated in the CDR and the value used to determine the momentum kick is taken by randomly sampling a gaussian distribution that has this characteristic width. Because the hadron beam is rotated with respect to the z-axis of the solenoid (in both the x and y directions), the momentum deviations found in the beam frame are rotated into the detector frame. No such step is needed for the lepton beam divergences.

Figure 7: The hadron beam x-component of momentum vs the z-position of the interaction vertex for the 18x275 GeV 25 mRad (upper left), 18x275 GeV 35 mRad (upper right), 5x41 GeV 25 mRad (lower left), and 5x41 35 mRad (lower right) configurations. The bunch crabbing rotation introduces a differential momentum kick in the x-direction depending on the z-position of the colliding particle within the bunch. This is then correlated with z-position of the collision vertex in the detector frame.

The final beam effect considered in this model is the transverse momentum kick introduced by the crabbing rotation. The size of this kick on an individual particle varies as a function of the distance along z of that particle from the center of its bunch. Particles at the center of the bunch do not receive a kick, while those at the head and tail of the bunch receive the largest kicks. The magnitude of this kick is given by the beam energy multiplied by Sine of the transverse offset angle, δ, which is given by:

$$\delta = \frac{\frac{\theta_c}{2}z}{\sqrt{\beta_{\mathrm{crab}}\beta^*}}. \tag{11}$$

Here, θ_c is the crossing angle, z is the distance of the interacting particle from the center of its bunch, β^* is the beta function at the IP taken from the CDR, and β_{crab} is the beta function at the crab cavity which can be found in Tabs. 1 and 2. The dependence of the magnitude of the transverse kick as a function of the z position of the particle within the bunch translates into a variation of the magnitude of the x component of the beam momentum as a function of the z position of the interaction as seen in Fig. 7.

The impacts on the x and y components of the hadron beam momentum from the four beam effects described above are summarized in Fig. 8 for the four beam energy and crossing angle combi-
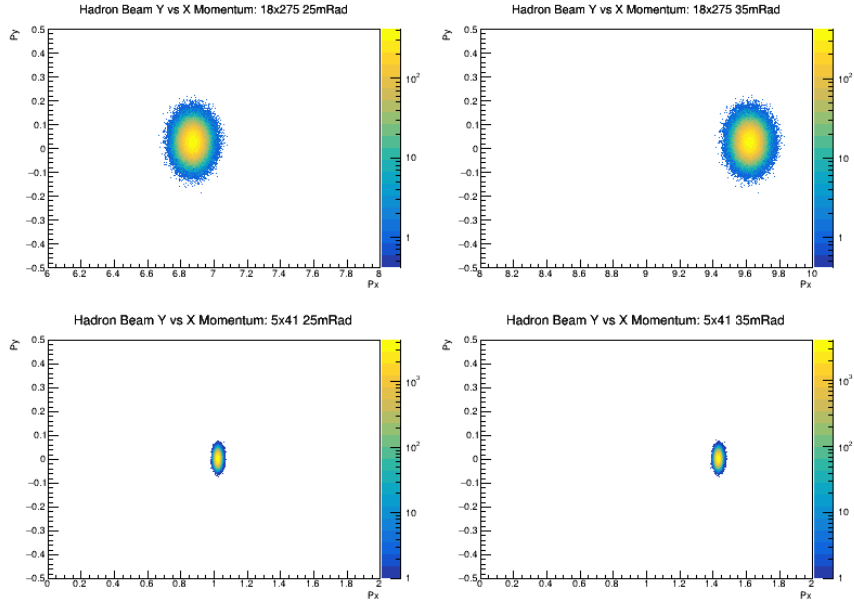
Figure 8: The y-component vs the x-component of the incoming hadron beam momentum for the 18x275 GeV 25 mRad (upper left), 18x275 GeV 35 mRad (upper right), 5x41 GeV 25 mRad (lower left), and 5x41 35 mRad (lower right) configurations. The offset in x-momentum is due to the crossing angle while the size of the distribution represents momentum smearing from beam divergence and crabbing effects.

nations. The offsets from zero in p_x (and the much smaller offsets in p_y) are a result of the crossing angle and are proportional to the beam energy and crossing angle. Therefore, the p_x offsets are larger for larger energies and larger crossing angles as seen. The widths of the distributions are driven by the angular divergence, which like the crossing angle itself, scales with the beam energy. The beam energy variation and crabbing kick effects also contribute to the widths, but at a much smaller level.

The changes to the beam momenta summarized above will effect the distribution of final state particles in the central detector region. The primary impact on the final state distributions comes from the crossing angle in the xz plane that leads to a concentration of particles at $\phi = 0$ and a pseudorapidity which depends on energy and crossing angle. The $\eta - \phi$ correlations for all final state particles from the four energy and crossing angle combinations can be seen in Fig. 9. The projections along the η and ϕ axes can be seen in Fig. 10. These figures also contain the distributions as they would appear assuming a head-on collision (no crossing angle) for comparison. The azimuthal distribution of particles is flat for the head-on collision case, but shows a strong peak to the direction of the outgoing hadron beam when the crossing angle is introduced. From the pseudorapidity projection, several features are evident. First, the crossing angle acts to move particles from high pseudorapidity into peaks at lower η. The peaks move to lower pseudorapidity for larger crossing angle and become more prominent at higher energy. As the hadron beam becomes more relativistic, the peak approaches the pseudorapidity of the beam direction (a crossing angle of 25 milliradians corresponds to a pseudorapidity of roughly 4.4). Finally, one sees that the distributions for different crossing angles (0, 25, and 35 milliradians) become degenerate for particles at smaller pseudorapidities indicating that the effects of the crossing angle are isolated to the pseudorapidity region around the peak. Although not shown explicitly, the azimuthal distribution indeed becomes flat at lower pseudorapidity.
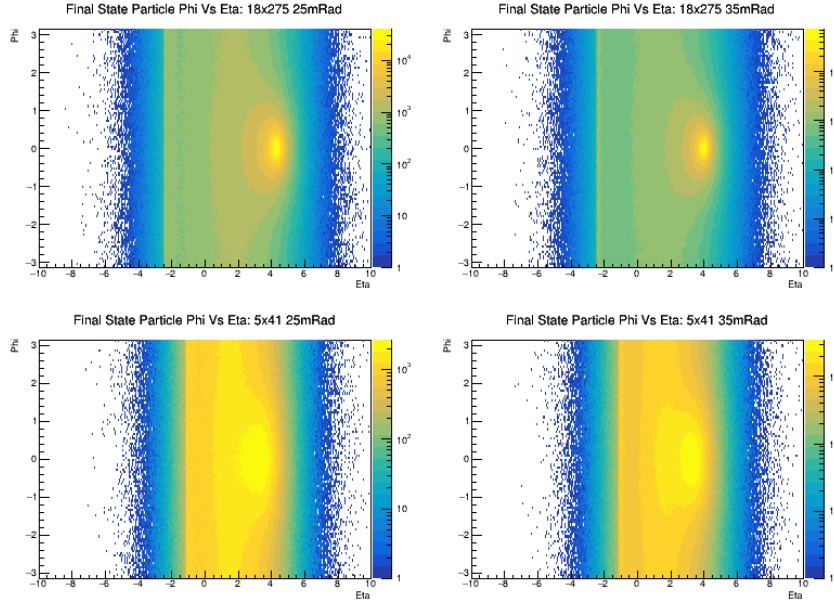
12

Figure 9: Final state particle azimuth vs pseudorapidity for the 18x275 GeV 25 mRad (upper left), 18x275 GeV 35 mRad (upper right), 5x41 GeV 25 mRad (lower left), and 5x41 35 mRad (lower right) configurations.

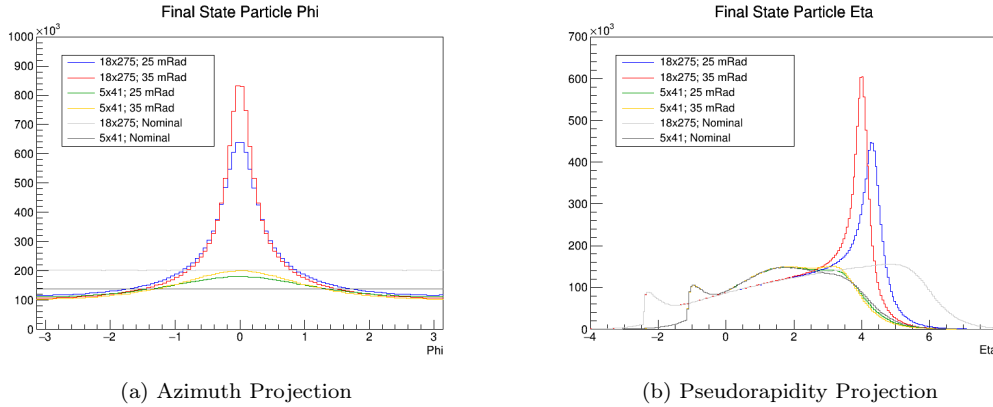(a) Azimuth Projection

(b) Pseudorapidity Projection

Figure 10: Final state particle azimuth (a) and pseudorapidity (b) distributions for the four beam energy and crossing angle combinations. Colored lines show the distributions with all beam effects included , while the grayscale lines show the distributions obtained from the head-on collisions with no other beam effects included.

In addition to changes in the $\eta - \phi$ positions of particles, the changes in beam momentum will also affect the final state particles' momentum. Figure 11 shows particle transverse momentum as a function of pseudorapidity for the four beam energy and crossing angle combinations as well as the distributions as they are when no beam effects are included. It is seen (especially for the higher hadron beam energy) that the particles at large pseudorapidity which are shifted into peaks at lower pseudorapidities are also pushed to higher transverse momentum. As with the pseudorapidity and

13

azimuthal distributions, the transverse momentum distribution is unaltered at lower pseudorapidity, away from the peaks.

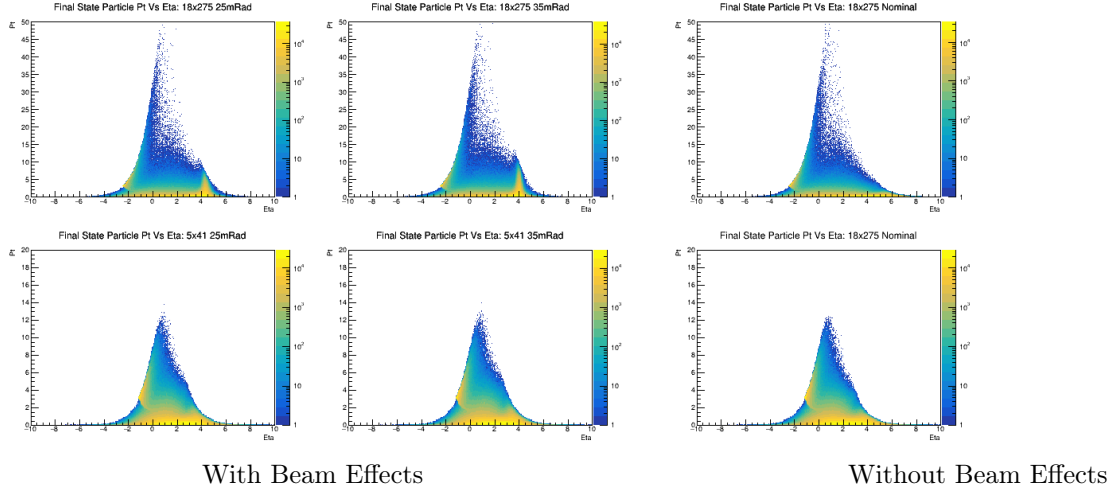With Beam Effects   Without Beam Effects

Figure 11: Final state particle transverse momentum vs pseudorapidity for the four beam energy and crossing angle combinations with beam effects included (a) and for head-on collisions at the two beam energies with no other beam effects included (b).

3.1.1 Coordinate Conventions

The PYTHIA-8 implementation described above assumes the electron beam travels in the negative z direction $(0, 0, -1)$ in the absence of divergence and crabbing effects and that the hadron beam travels in the positive x direction $(\text{Sin}(\theta), 0, \text{Cos}(\theta))$ where θ is the full beam crossing angle. Furthermore, the azimuthal coordinate ϕ is defined such that $\phi = 0$ lies along the positive x direction with $\phi = \pi$ along negative x and $\phi = +(-)\pi/2$ along the positive (negative) y directions.

There will be two interaction regions at the EIC: IP6 and IP8. For IP6, the beams will enter the interaction region from ring inside and exit to ring outside, while the opposite is true for IP8. Therefore, at IP8, the PYTHIA-8 implementation convention described above is compatible with a coordinate system in which the z axis points anti-parallel to the electron direction of travel, the y axis points to the sky, and the x axis points toward the inside of the ring. This is a right-handed coordinate system. At IP6, the convention holds for a coordinate system in which the z and y axes again point in the negative electron and upward directions, respectively, but the x axis points to ring outside. This is a left-handed coordinate system. It is of course a matter of convention what coordinate system the experiments at each interaction region adopt, but shifting the direction of the x axis will simply move the final particle hot-spot from $\phi = 0$ to $\phi = \pi$.

3.2 Generator Agnostic After-burner

We recognize not all the diverse EIC event generators would intrinsically support the beam crossing angle and beam effects. In addition, the users may opt to use the same set of head-on collision generator events for simulations in various scenarios of beam crossing angle and divergence tunings. Therefore, we also introduced a Generator Agnostic After-burner, that translates the generator events from the head-on collision frame to the lab frame via a position translation and a Lorentz-rotation. One implementation of this After-burner was implemented in the Fun4All-EIC software

distributions (detailed in Section A.2) and showed excellent agreement with the PYTHIA-8 Implementation as discussed in Section 3.3.
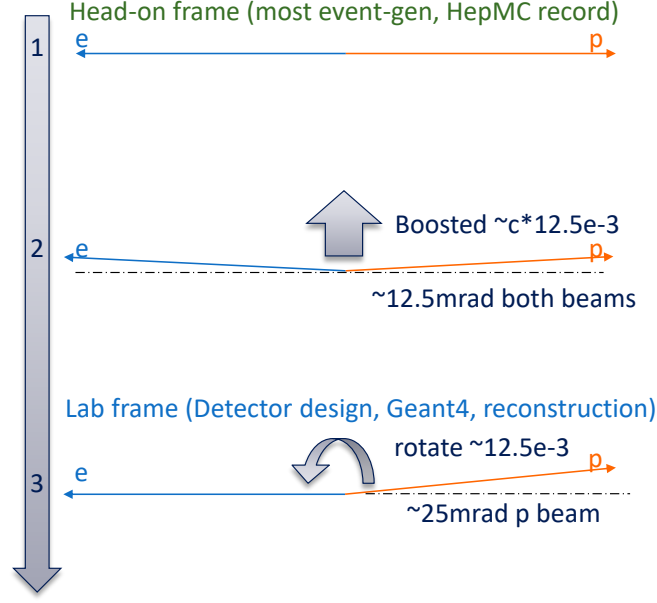
3.2.1 Algorithm Description

Figure 12: An illustration of the steps introducing 25 mrad beam crossing angle from a head-on frame of an event generator to the lab frame. Note the numbers in this illustration are approximations as there is collision-by-collision variation from beam divergence and crab cavity kick that perturbate these parameters collision-by-collision at a smaller level, O(100) μrad.

The cartoon steps introducing beam crossing angle, $\theta_{CA} = 25$ mrad, from a head-on frame of an event generator to the lab frame is illustrated in Figure 12:

1. The algorithm input is the generator event described as a list of the four momenta of each final state particle in the head-on frame. In Figure 12, only the three vectors of the electron and proton beam are shown for simplicity and clarity purposes.

2. The head-on frame is first boosted sideways, perpendicular to the head-on colliding beam, and towards the beam crossing direction. The amplitude of the boost is $ctan(\theta_{CA}/2)$, if ignoring the beam divergence and crab-cavity kick. In the presence of these variations, the final boost direction and amplitude are chosen according to the final angle between the two beams at the lab frame.

   - Note for relativistic beams, this boost is independent of the beam energy, which dramatically simplified the implementation.
   - Please also note the beam energy is not Lorentz invariant. This choice of the boost vector induces minimal changes in the beam energies of both beams between the two frames, i.e.

$$E_{\text{lab}} = E_{\text{head-on}}/cos(\theta_{CA}/2)$$

15

3. In the last step, a simple rotation of $\theta_{CA}/2$ around the vertical axis aligns the electron beam back to the $-z$ axis, which leaves the proton beam with the intended crossing angle of θ_{CA}. In the presence of the beam divergence and crab-cavity kick, the final rotation angle is $arccos(-\hat{p}_p \cdot \hat{p}_e)/2$ and the rotation axis is $\hat{p}_p \times \hat{p}_e$, where $\hat{p}_p$ and $\hat{p}_e$ are the final unit vector of the hadron and electron beam directions, respectively.

These boost and rotation operations can be encoded conveniently in a single transform matrix, such as a
`CLHEP::HepLorentzRotation`, and be applied to all four vectors of an event generator record, as linked in Section A.2

In addition to boosts and rotations to momentum vectors, the after-burner should also handle the stochastic shift of the collision vertex, following the algorithm outlined in Section 3.1. Please note that the vertex simulation will also give the crab momentum kick to the beam particle, which will input to the final true beam particle's direction in the lab frame, and therefore it is part of the input to the boost and rotation calculation.

3.2.2 Limitations and Discussions

As this Generator Agnostic After-burner utilizes Lorentz-rotation to translate four vectors from a generator's head-on collision frame to the lab frame, Lorentz invariant variations cannot be introduced via this method. Notably, the slight variation of the center of mass energy, $\sqrt{s_{ep/N}}$, that stems from the beam energy spread of both beams can not be altered in the After-burner.

As the beam energy variation is small, ranging relatively from 10^{-4} to 10^{-3} as in Table 4, this effect is small for most wide-phase-space reactions as SIDIS as quantified in Section 3.3. However, we suspect such an effect may be important for exclusive or on-threshold productions. To properly simulate such events with this after-burner, the users should introduce beam energy variation in the event generator, such as by allowing beam energy to vary if supported by the event generator, or stage a set of files with varying beam energies and properly mix the events in the analysis to reproduce the beam energy profile.

3.3 Comparison

The PYTHIA-8 and after-burner implementations described above should provide equivalent descriptions of the final state particle distributions, modulo differences arising from the fact that the after-burner method does not include effects from the beam energy variation (should be small). In order to ensure this is the case, final state particle pseudorapidity and azimuthal distributions were compared in Figures 13, 14, 15, and 16. These comparisons cover the combinations of 25 and 35 mrad crossing angles, and beam energies combinations of 18×275 and 5×41 GeV, which is aimed to cover the max ranges of the envisioned EIC program envelop. Care was needed to ensure all particle cuts were consistent between the two methods (no inelasticity cuts or cuts on the scattered electron) and that potential long-lived particle decays were not excluded from the afterburner sample. In the η distributions, we note the peak in the negative η which stems from the kinematics cut off of the DIS electron. We also note in the high beam energy settings (Figures 13 and 14), a distinct peak emerges at the η that corresponding to the beam crossing angle, which present a tightly collimated target fragmentation jet.

The ratio between PYTHIA-8 and after-burner implementations are shown in the right panels of Figures 13-16, which quantify the difference between the two methods. In all four beam configurations, we observed excellent agreement on the particle distributions up to the statistical precision of O(1)M event sample and well below 1% in the relative difference. This also demonstrated the beam energy smear, which is implemented in PYTHIA-8 but can not be introduced via the after-burner, is a small effect for SIDIS process, although it may be visible in exclusive or on-threshold production channels.
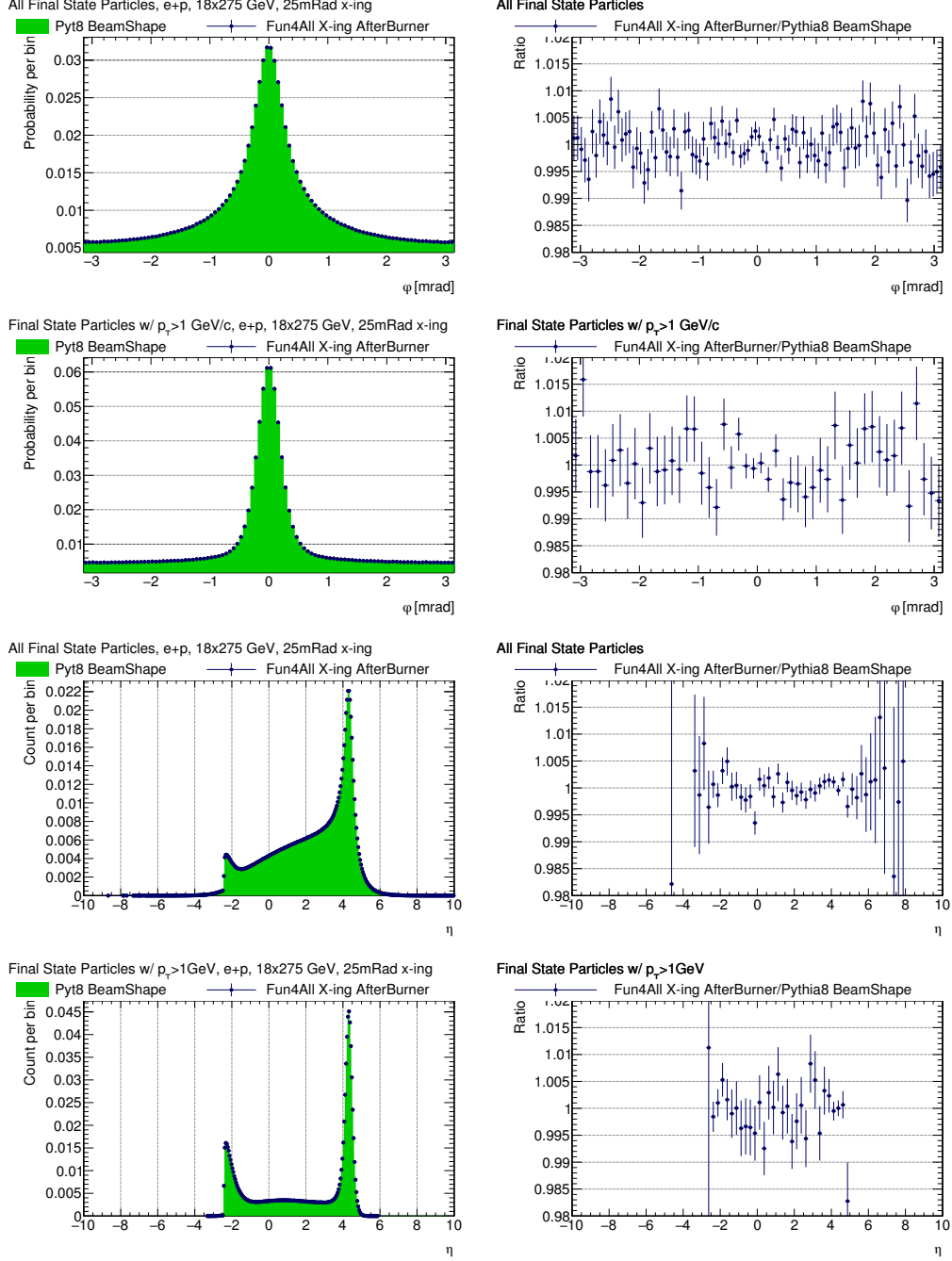
Figure 13: Final state particle distribution of the $e + p$ 18×275 GeV SIDIS events with 25 mrad crossing angle, shown as the comparisons between the implementations of PYTHIA-8 BeamShape (left green shade), Fun4All After-Burner (left blue data point), and their ratios (right column). First row: all particles as function of ϕ; second row: particles with $p_T > 1$ GeV/c as function of ϕ; third row: all particles as function of η; last row: particles with $p_T > 1$ GeV/c as function of η
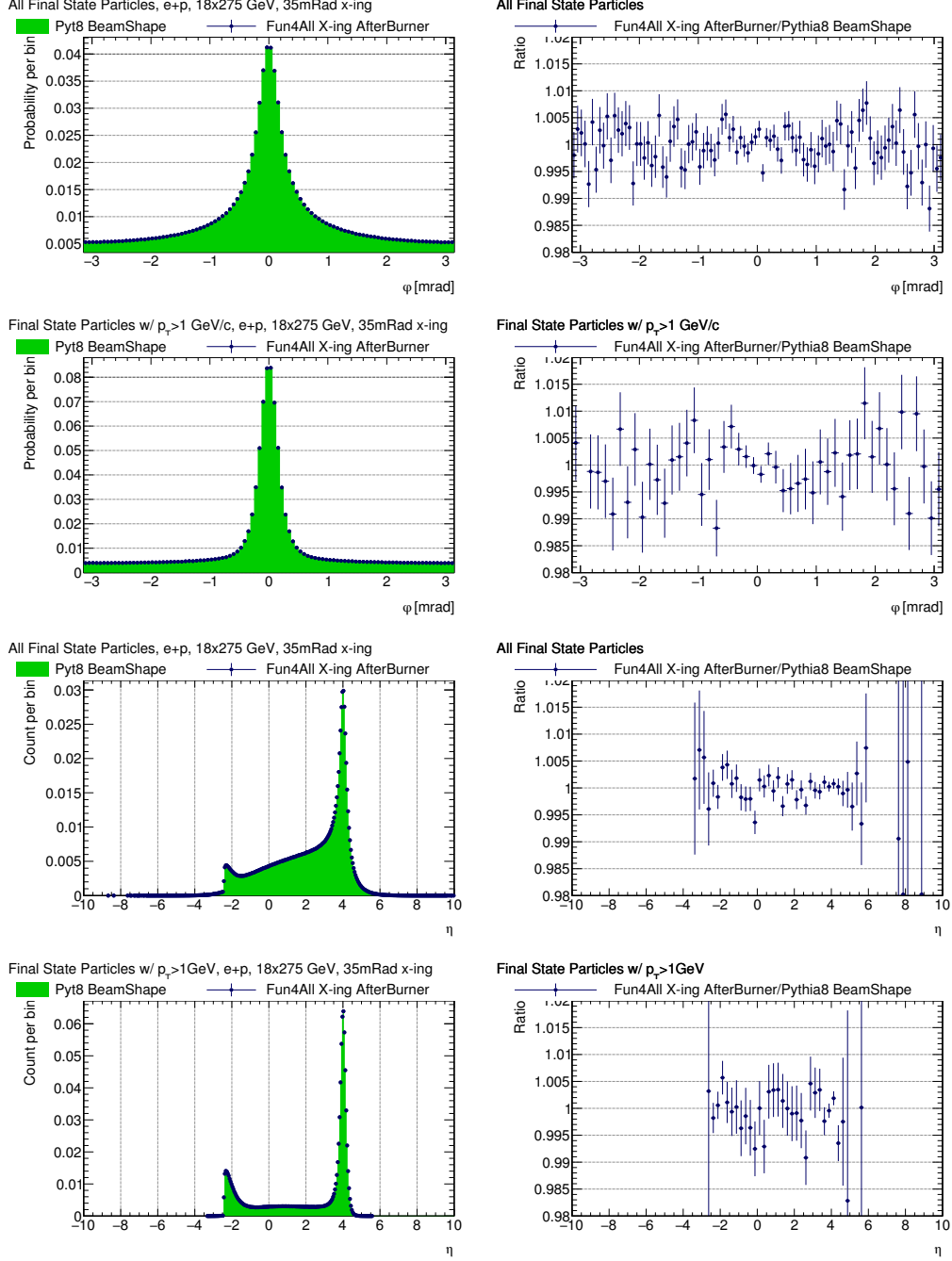
Figure 14: Final state particle distribution of the $e + p$ 18×275 GeV SIDIS events with 35 mrad crossing angle, shown as the comparisons between the implementations of PYTHIA-8 BeamShape (left green shade), Fun4All After-Burner (left blue data point), and their ratios (right column). First row: all particles as function of ϕ; second row: particles with $p_T > 1$ GeV/c as function of ϕ; third row: all particles as function of η; last row: particles with $p_T > 1$ GeV/c as function of η
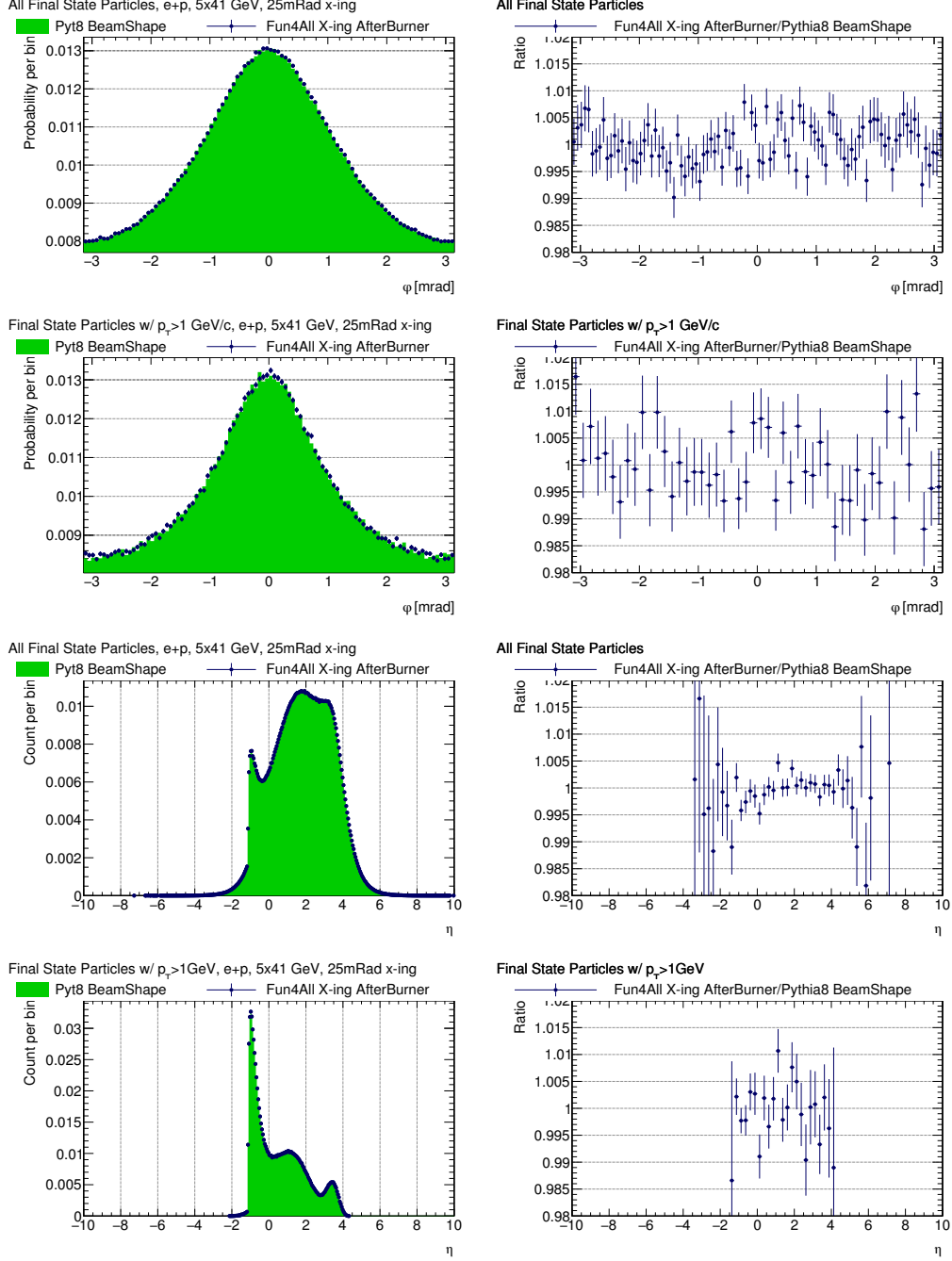
18

Figure 15: Final state particle distribution of the $e + p$ 5×41 GeV SIDIS events with 25 mrad crossing angle, shown as the comparisons between the implementations of PYTHIA-8 BeamShape (left green shade), Fun4All After-Burner (left blue data point), and their ratios (right column). First row: all particles as function of ϕ; second row: particles with $p_T > 1$ GeV/c as function of ϕ; third row: all particles as function of η; last row: particles with $p_T > 1$ GeV/c as function of η
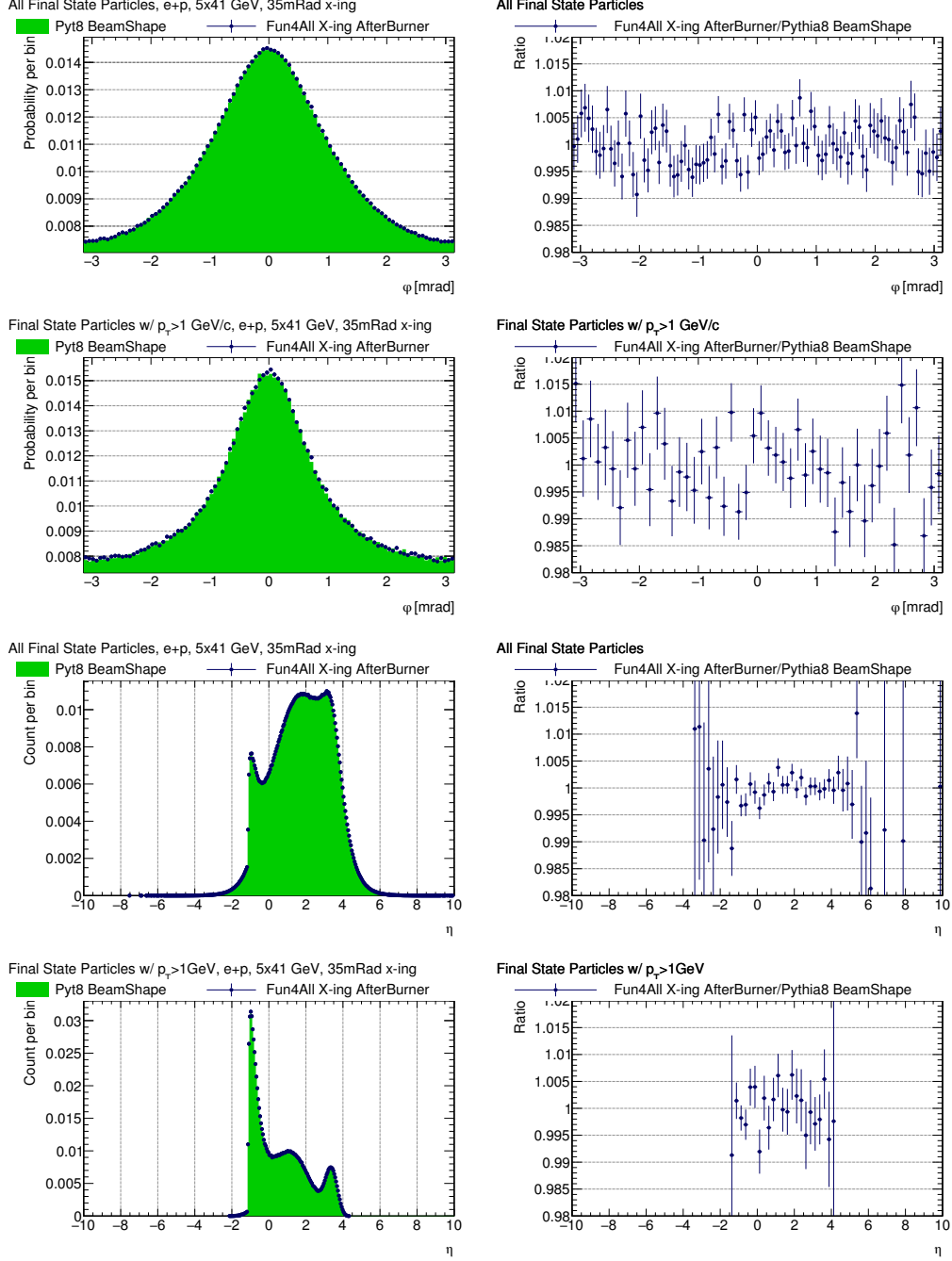
Figure 16: Final state particle distribution of the $e + p$ 5×41 GeV SIDIS events with 35 mrad crossing angle, shown as the comparisons between the implementations of PYTHIA-8 BeamShape (left green shade), Fun4All After-Burner (left blue data point), and their ratios (right column). First row: all particles as function of ϕ; second row: particles with $p_T > 1$ GeV/c as function of ϕ; third row: all particles as function of η; last row: particles with $p_T > 1$ GeV/c as function of η

3.4 Transport model for primary vertex size

Precise knowledge of primary vertex distribution is one of requirements for the design of the luminosity monitor. A model based on transport of protons or Au ions and electrons through the interaction point was developed to address the question of vertex spread in presence of the crabbing effects. Furthermore the results provide an independent cross check to the PYTHIA-8 implementation.

The model creates electron and proton or Au ion bunches at a time before the collision. Particles in bunches have a Gaussian distribution with the width in x and y as $\sqrt{\text{RMS emittance} \times \beta^*}$, the width in z is given by the RMS bunch length. Crossing angle of 25 mrad and ESR vertical shift of 100 µrad are both considered when the bunches are created. Crabbing is implemented by rotating both bunches by a half of the crossing angle. An approximation is made by considering the angle of each bunch as fixed during the collision.

Expected vertex distribution is obtained by integrating the overlap of the bunches as they pass through the interaction point. To make the calculation, space in x, y and z around the interaction point is divided into a small volumes. Then the bunches are transported in steps in time through the interaction point. Overlap in electron and proton or Au ion bunches is calculated at each time step in each volume. The overlap of bunches is quantified by intersection in number of electrons and protons or Au ions in each particular volume; e.g. with 3 electrons and 10 protons the overlap is 3. A video in https://indico.bnl.gov/event/12197/contributions/50972/attachments/35263/57390/ep-18x275-Tab3p3.mp4 shows electron and proton bunches at 18x275 GeV passing through the interaction and the actual overlap in xy plane and along z is given there.

Evolution in bunch overlap in time steps is integrated over the time. The overlap along a particular x, y or z coordinate is obtained by integrating over the other two coordinates.

The resulting vertex distribution for 18x275 GeV ep beams is shown in Fig. 17. The plots give a Gaussian fit to the calculated bunch overlap along the individual coordinates. The width of the Gaussian $\sigma_{x,y,z}$ gives the expected size of the primary vertex. The model was configured according to the CDR Table 3.3.
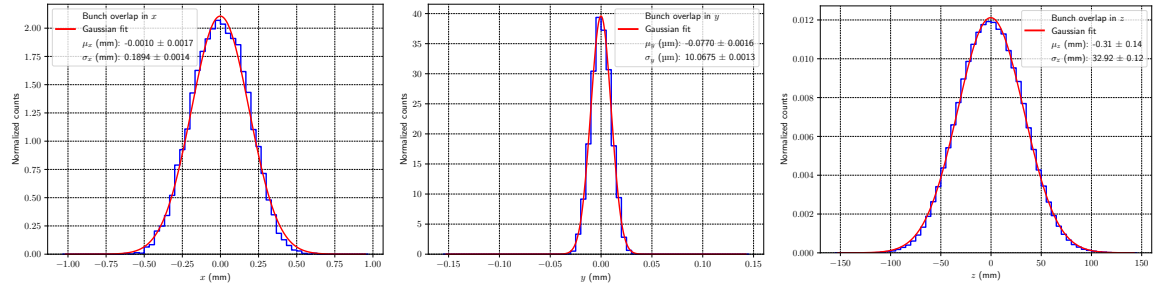

Figure 17: Expected primary vertex distribution for ep at 18x275 GeV as obtained from the transport model, assuming the CDR Table 3.3 beams configuration.

The results for other beam energies and for Au ion beams are given in Tab. 3. For electron - proton beams the CDR Table 3.3 was used to configure the model, the electron - Au ion beams were configured according to CDR Table 3.5.

The width of primary vertex in x, σ_x is much larger than the width in y, σ_y as a result of the crossing angle and crabbing. Both are slightly increasing with decreasing ep energies while they remain about the same in e-Au. The width in z, σ_z shows increasing trend with decreasing energies for both beam species. The error in each value is the uncertainty from the Gaussian fit. Systematic checks have been performed by varying the number of electrons and protons representing the bunches, showing consistent results.

Good agreement has been found between the transport model and PYTHIA-8 implementation,

Species, energy (GeV)		Vertex size	Transport model	PYTHIA-8
proton 275	electron 18	σ_x (mm) σ_y (µm) σ_z (mm)	0.1894 ± 0.0014 10.0675 ± 0.0013 32.92 ± 0.12	0.1403 ± 0.0001 8.0173 ± 0.0056 30.24 ± 0.02
proton 100	electron 10	σ_x (mm) σ_y (µm) σ_z (mm)	0.2057 ± 0.0023 12.2144 ± 0.0018 36.00 ± 0.15	0.1313 ± 0.0001 8.0221 ± 0.0057 35.13 ± 0.02
proton 41	electron 5	σ_x (mm) σ_y (µm) σ_z (mm)	0.2429 ± 0.0020 25.0197 ± 0.0060 37.77 ± 0.28	0.1649 ± 0.0001 19.0005 ± 0.0134 37.62 ± 0.03
Au ion 110	electron 18	σ_x (mm) σ_y (µm) σ_z (mm)	0.3210 ± 0.0035 15.1721 ± 0.0025 36.00 ± 0.07	
Au ion 41	electron 5	σ_x (mm) σ_y (µm) σ_z (mm)	0.3130 ± 0.0022 15.3381 ± 0.0048 59.91 ± 0.36	

Table 3: Results on expected primary vertex size from the transport model for ep and e-Au beams and comparison to PYTHIA-8.

as can be seen from comparison made in Tab. 3. The results obtained by the transport model are consistently above the PYTHIA-8, and can be considered as an upper limit to the primary vertex size.

4 Conclusion

Measurements at the EIC will be influenced by various accelerator and beam effects: the crossing angle, the crabbing rotation, the beam energy spread, the angular beam divergence, and the bunch length. We describe these effects in Sec. 2 and study their influence on the space-time position of the collision vertex and the momenta of the incoming electron and ion beams in detail in Sec. 3. The largest change on the incoming beam momenta and - as a consequence - on the distribution of the final-state particles arises from the crossing angle. While the lepton beam in unaffected, the ion beam receives a kick in the x direction with a magnitude given by the beam energy multiplied by the sine of the full crossing angle. The accelerator and beam effects also change the $\eta - \phi$ positions of the final-state particles. This also affects their azimuthal distribution, which instead being flat as in case of head-on collisions shows a peak in the direction of the outgoing ion beam. The accelerator and beam effects we have studied need to be included in physics and detector simulations for the EIC. They can have profound consequences of the measurement capabilities of the EIC and the design and layout of the detectors. Of particular interest are, e.g., analysis of azimuthal modulations in the cross section that reveal insights on GPDs or TMDs and the possible fake asymmetries being caused by the accelerator and beam effects.

In our studies, we demonstrate that the accelerator and beam effects can be also studied by modifying the Monte Carlo input to detector simulations, without having to implement the effects directly in the event generators. This generator-agnostic approach can be implemented as a standalone program or as part of the detector simulation tools that are being used for the EIC. Only changes due to the beam energy spread cannot be included in this approach and need to the taken

Table 4: Parameters used in the PYTHIA-8 implementation taken from Table 3.3 in the CDR. The designations h and v stand for horizontal (x direction) and vertical (y direction).

Species	Proton	Electron	Proton	Electron	Notes
Energy [GeV]	275	18	41	5	
RMS Emittance h/v [nm]	18/1.6	24/20	44/10	20/3.5	Used with β^* to determine bunch size
β^* h/v [cm]	80/7.1	59/5.7	90/7.1	196/21	Used with emittance to determine bunch size
RMS $\Delta\theta$ h/v [μrad]	150/150	202/187	220/380	101/129	Used to determine angular beam divergence
RMS Bunch Length [cm]	6	0.9	7.5	0.7	Used in vertex calculation
RMS $\frac{\Delta p}{p}$ [10^{-4}]	6.8	10.9	10.3	6.8	Used to set beam energy spread

into account at generator level or by properly mixing Monte Carlo files with varying beam energies.

For the simulations of the impact of the accelerator and beam conditions on the measurements at the EIC, the correct magnitudes of the various effects need to be used. The implementations described in this note use the beam parameters as documented in the EIC Conceptual Design Report in Tables 3.3 – 3.5. In our studies, we focus on electron-proton collisions at the two limiting beam energy combinations, 18x275 GeV and 5x41 GeV, in the high divergence configuration (Tab. 3.3). The PYTHIA-8 implementation also handles energy combinations of 10x275 GeV, 10x100 GeV, and 5x100 GeV, as well as the high acceptance configuration (Tab. 3.4). The PYTHIA-8 implementation does not yet handle beam parameters for heavy ion running (Tab. 3.5), but they can easily be added. The relevant beam parameters for the two beam energies in the high divergence configuration are reproduced in Tab. 4 along with a brief description of their use.

A Code Location

A.1 PYTHIA-8 Implementation

The PYTHIA-8 implementation described above is available on GitHub. There are two branches in this repository: 'master' and 'headonTestJin'. Both contain the same implementation of the PYTHIA-8 beam effect code, but the analysis code for generating performance/diagnostic plots in 'master' contains several event and particle cuts which would be appropriate for jet or SIDIS analyses. The analysis code in 'headonTestJin' removes these cuts so a faithful comparison with the After-burner implementation can be made.

A brief description of the code in the repository is below:

- eicBeamShape.h/cxx: This code defines the vertex model and beam shape modifications

- PythiaBeamShape.cxx: Code to run PYTHIA and generate performance/diagnostic plots in root

- PythiaBeamShapeHepMC.cxx: Code to run PYTHIA with beam effects and write output to a HepMC (version 2) file

- steerFiles: Directory which contains steering files for running various EIC beam energies and high divergence or acceptance settings with proper accelerator parameters

A.2 Generator Agnostic After-burner

One implementation of the Generator Agnostic After-burner is implemented in the Fun4All EIC software, which is detailed as following:

- The Pull Request introducing and carries the Generator Agnostic After-burner is at https://github.com/sPHENIX-Collaboration/coresoftware/pull/1087.

- The core function performing the boost-rotation calculation, `void PHHepMCGenHelper::`⌋ `HepMC2Lab_boost_rotation_translation(PHHepMCGenEvent *genevent)`, is located at PH-HepMCGenHelper.cc#L164. It can be reviewed with the EIC Doxygen Code Reference at a0148635f83f76e3f6cee429a8de49fbd. It is part of the daily CVMFS distribution.

- The application of frame transform from HepMC genertor event to the lab frame in Geant4 input is performed at `int HepMCNodeReader::process_event(PHCompositeNode *topNode)` at HepMCNodeReader.cc#L214.

- Example macros setup beam parameters for any HepMC-compatible event generator inputs: `void ApplyEICBeamParameter(PHHepMCGenHelper *HepMCGen)` at G4_Input.C#L116 or can be viewed with the EIC Doxygen Code Reference a0d3ec00dcd31f521d5b88a044e5a9aff.

- The source code and comparison plots Fig. 13, 14, 15, and 16 are published as Jupyter notebooks which can be viewed conveniently with https://nbviewer.jupyter.org/github/ECCE-EIC/analysis/tree/0f38849/BeamXingCheck/.

A.3 Transport model

The source code of the transport model for the primary vertex size, as described in Sec. 3.4 is available on GitHub. A brief description is as follows:

- `run.py`: macro to run the simulation

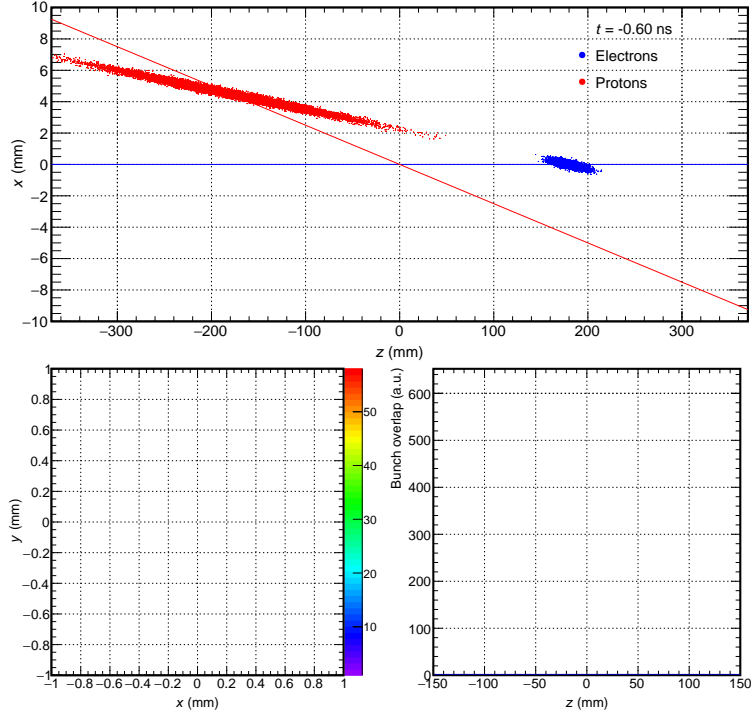- `cards/`: directory containing steering cards

Figure 18: Initial state, both bunches are approaching the IP.

- `bunch.cxx/h`: bunch representation

- `sim.cxx/h`: simulation implementation

- `macro/fit_xyz.py::` Gaussian fits to vertex shape

- `python/`: directory with helper functions

The .cxx/h files are located in `src` and `include` directories.

B   Movie showing evolution in bunch overlap during the interaction

A movie showing electron and proton bunch movement during their interaction has been taken from the transport model (Sec. 3.4). The visualization is for an electron-proton collision at 18x275 GeV.

The series of plots in Fig. 18 – 20 provide snapshots of the movie from a time before the interaction (Fig. 18), time when both bunches are located at the origin (Fig. 19) and a time when both bunches are leaving the interaction (Fig. 20). The top panel in each plot shows the layout in the xz plane with the blue line representing the direction of the electron beam and red line the direction of the proton beam, taking the full crossing angle of 25 mrad into account. Electrons and protons forming the bunches are shown as given in the legend. The bottom two panels give the actual bunch overlap at a given time in the xy plane and along the z axis.
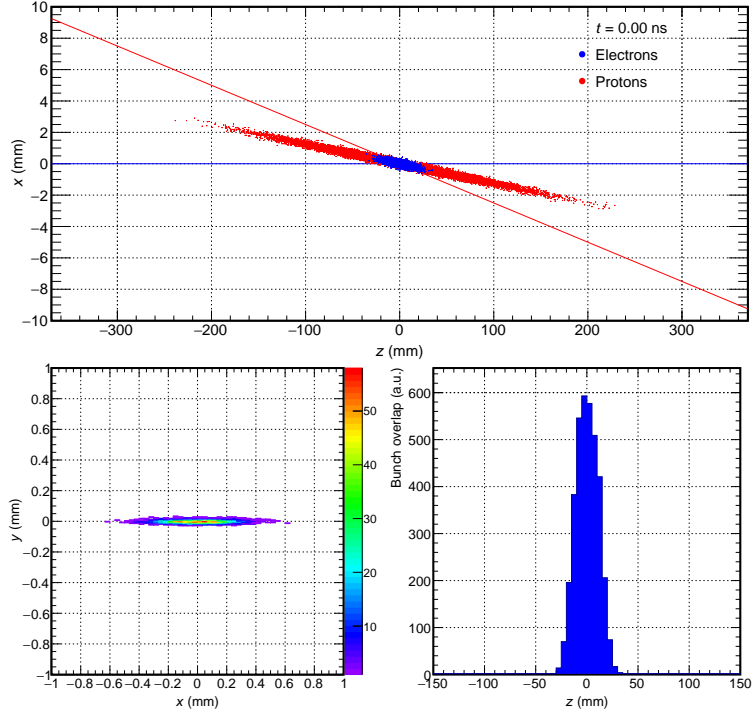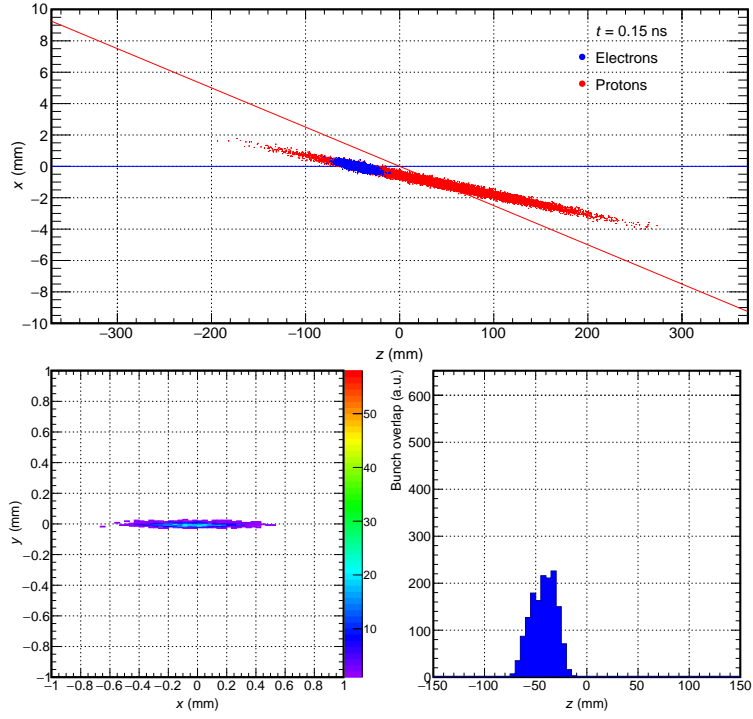
Figure 19: Bunches are located at the origin.

Figure 20: Bunches are moving away from the IP.